SOIL DYNAMICS AND EARTHQUAKE ENGINEERING

Winkler model for lateral response of rigid caisson foundations in linear soil

Nikos Gerolymos, George Gazetas *

National Technical University, Athens, Greece

Accepted 3 December 2005

Abstract

A generalized spring multi-Winkler model is developed for the static and dynamic response of rigid caisson foundations of circular, square, or rectangular plan, embedded in a homogeneous elastic. The model, referred to as a four-spring Winkler model, uses four types of springs to model the interaction between soil and caisson: lateral translational springs distributed along the length of the caisson relating horizontal displacement at a particular depth to lateral soil resistance (resultant of normal and shear tractions on the caisson periphery); similarly distributed rotational springs relating rotation of the caisson to the moment increment developed by the vertical shear tractions on the caisson periphery; and concentrated translational and rotational springs relating, respectively, resultant horizontal shear force with displacement, and overturning moment with rotation, at the base of the caisson. For the dynamic problem each spring is accompanied by an associated dashpot in parallel. Utilising elastodynamic theoretical available in the literature results for rigid embedded foundations, closed-form expressions are derived for the various springs and dashpots of caissons with rectangular and circular plan shape. The response of a caisson to lateral static and dynamic loading at its top, and to kinematically-induced loading arising from vertical seismic shear wave propagation, is then studied parametrically. Comparisons with results from 3D finite element analysis and other available theoretical methods demonstrate the reliability of the model, the need for which arises from its easy extension to multi-layered and nonlinear inelastic soil. Such an extension is presented in the companion papers by the authors [Gerolymos N, Gazetas G. Development of Winkler model for lateral static and dynamic response of caisson foundations with soil and interface nonlinearities. Soil Dyn Earthq Eng. Submitted companion paper; Gerolymos N, Gazetas G. Static and dynamic response of massive caisson foundations with soil and interface nonlinearities—validation and results. Soil Dyn Earthq Eng. Submitted companion paper.].
© 2006 Elsevier Ltd. All rights reserved.

Keywords: Caisson; Winkler model; Elasticity; Lateral loading; Kinematic loading; Seismic loading

1. Introduction

Caisson foundations deeply embedded in soft soil have been widely used to support major structures, especially bridges. Monumental examples are the Tagus bridge in Portugal, supported on perhaps the tallest (88 m high) caisson in the world; the San-Francisco-Oakland bay bridge whose major pier is founded on a 75 m high caisson; the Williamsburg and Verrazano Narrows bridges in New York; the Port island and Nishinomiya-ko bridges in Japan, the massive caissons of which played a major role in the survival of these bridges during the Kobe 1995 earthquake [3]. Despite their large dimensions, caisson foundations have been shown not to be immune to seismic loading as it was believed for many years. This was confirmed in the Kobe (1995) earthquake, which caused many structures founded on caissons to suffer severe damage.

The lateral and seismic response of deep foundations has been of considerable interest for many years. A number of methods of varying degrees of accuracy, efficiency and sophistication have been developed. However, only few of them are devoted to caissons. Instead, the methods of solution developed for (rigid) embedded foundation and for (flexible) piles have been frequently adapted to deal with the caisson problem. A partial list of such methods would include (in crudely-chronological order): the analytical solution of Tajimi [4] for a cylindrical foundation embedded in a stratum and bearing on bedrock; the versatile approximate analytical solutions of Novak and Beredugo [5]; the 'consistent-boundary' finite element formulations of Kausel and Roesset [6] for circular foundations in layered deposits over bedrock; the boundary element solution for rectangular foundations in a halfspace by Dominguez [7]; the semi-numerical formulation of Tassoulas [8] applied to embedded cylindrical foundations with variable sidewall heights; the time-domain boundary element method of Karabalis and Beskos [9]; the hybrid boundary-element and finite element

solution of Mita and Luco [10] for square foundations embedded in a halfspace; and the 'flexible-volume' substructuring technique of Tajirian and Tabatabaie [11]. Harada [12] developed an approximate analytical solution for cylindrical foundations combining Tajimi's and Novak's concepts. One of the most comprehensive studies on the seismic response of flexible and rigid caissons was conducted by Saitoh [13], who extended Tajimi's 1969 approximation to account for caisson flexibility and for soil and interface nonlinearities (separation and gapping of the caisson from the soil). He showed that Novak's plane strain approximation, logical as it may be, leads to inaccurate results.

Most of the above methods refer to cylindrical foundations. A comprehensive series of studies on the static and dynamic response of embedded rigid foundations having various plan shapes (ranging from rectangular of any aspect ratio to triangular) have been published by Gazetas, and co-workers [14–17]. Utilizing an efficient boundary-element method, and numerous results from the published literature, they developed closed-form semi-analytical expressions and charts for stiffnesses and damping of horizontally and rotationally loaded arbitrarily-shaped rigid foundations embedded in homogeneous soil [18]. Incomplete contact between the foundation vertical walls and the surrounding soil were taken into account in a crude way. Ample confirmation of the basic validity of some of the main concepts and results in these publications were recently provided by Gadre and Dobry [19] through centrifuge modeling.

However, the above-mentioned analytical expressions and charts cannot directly apply to multi-layered soils. Furthermore, it would be impossible to even crudely extend them for use with nonlinearly behaving soils, or to model realistically phenomena such as separation (gapping) and uplifting that may take place under strong static and seismic excitation. On the other hand, the widely available commercial finite-element and finite-difference computer codes, while in principle capable of treating soil nonlinearities, are not yet an easy solution when rectangular caissons are studied (requiring a 3D mesh), embedded in deep soil deposits and subjected to seismic shaking (both requiring special and very distant boundaries), and undergoing strong oscillations with the aforementioned interface nonlinearities (requiring special interface elements).

In an effort to bridge this apparent gap in the available methods and tools for analysis of lateral loaded caisson foundations, this paper along with the two companion papers by the present authors [1,2] develops a generalized Winkler type method described by four types of springs (and associated dashpots). Our aim is to provide, a sound engineering solution to the problem, with a method that has the following attributes:

(a) it provides the response to static, cyclic, and dynamic loading applied at the top of a caisson, as well as to seismic ground deformations ('kinematic' excitation);

(b) it models the full variety of caisson plan shapes that are usually encountered in practice (circular, square, rectangular, elliptical);

(c) it readily handles any horizontally layered soil profile (as well as continuously inhomogeneous soils);

(d) it treats both material (soil) inelasticity and geometric (interface) nonlinearities in an approximate but realistic fashion.

The present paper, the first in the sequence, develops an elastic 'four-spring' Winkler model and calibrates it with the aforementioned elastodynamic solutions (in the form of analytical expressions) of Ref. [18] for foundations embedded in a homogeneous elastic halfspace. The prediction of the model is satisfactorily compared with results from 3D-finite element analysis.

The subsequent companion paper [1] addresses the issue of soil and interface nonlinearities, and develops a versatile inelastic Winkler model in which each type of 'spring' is described through a nonlinear differential equation of the Bouc-Wen type.

The model is validated in the third companion paper [3] against results from (a) load tests, and (b) 3D finite element analysis, and is then utilised in a parameter study that sheds light on the role of material and geometric nonlinearities.

It is noted that in addition to the previously mentioned research, Davidson et al. [20] had also developed a four-spring Winkler model for rigid caissons, and calibrated it with 3D-finite element analysis, and static load tests. Also of related interest is the work of Mylonakis [23] who introduced the Vlasov-Leontiev 'Winkler-with-shear-layer' idealization to model: (a) the dynamic soil reaction against caissons, (b) the dynamic impedance of the caisson, and (c) the dynamic interaction between two neighboring caissons. He derived explicit closed-form solutions for a flexible large-diameter cylindrical shaft embedded in a homogeneous soil resting on a rigid base, for various boundary conditions.

2. The physics of the problem and a Winkler model

Our study deals with rigid caisson foundations. Their depth to width ratio is in the range of 0.5–3, depending on soil deformability. By contrast to piles, which are slender structures, with caisson foundations the lateral soil reaction is not the sole resisting mechanism. The shear tractions at the circumference of the caisson are also of considerable importance and must not be ignored in foundation response analysis. On the other hand, caissons differ from the usual embedded foundations (characterized by a depth to width ratio smaller than 1), the base of which provides most of, or even the only resistance to loading. Fig. 1 shows a crude classification according only to their geometry, ignoring the influence of soil stiffness, which is an equally important parameter.

Caisson–soil interaction is strongly related to the complex stress distribution along the caisson shaft. Fig. 2 shows the stress pattern for a caisson with (a) circular and (b) rectangular cross-section.

A dynamic Winkler four-spring model is developed in this paper incorporating distributed translational (lateral) and rotational (rocking) springs and dashpots, as well as concentrated shear translational (shear) and rotational (moment) springs and dashpots at the base of the caisson.
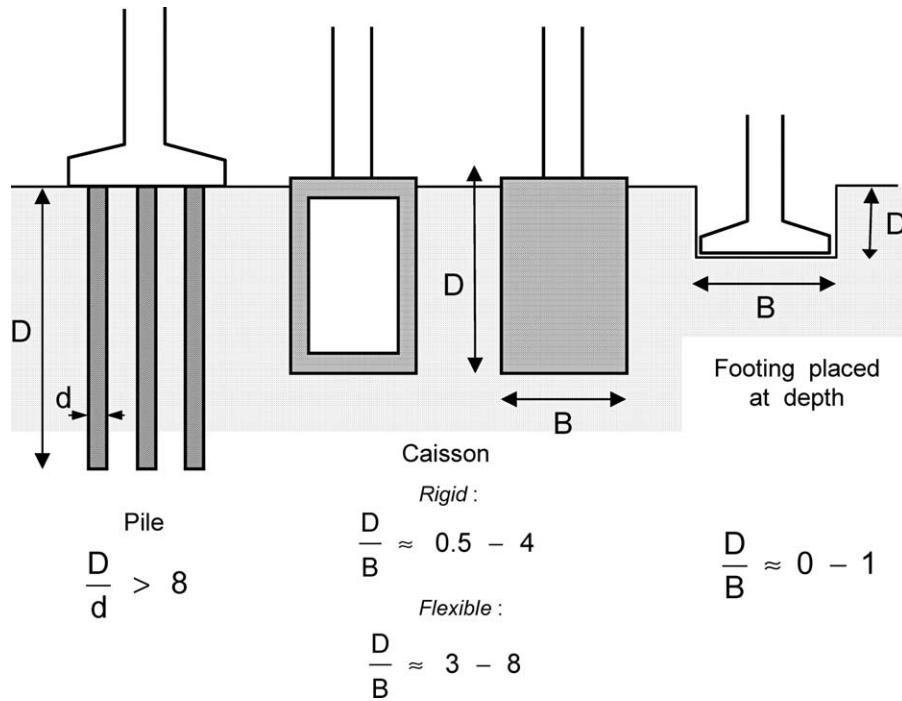
Fig. 1. A possible crude classification of foundations according to the slenderness or depth of embedment of their individual elements. (The flexibility of a caisson depends on whether it is massive or cellular; on the stiffness of the soil; and on the material of the caisson.)

These four types of springs and dashpots are related to the resisting forces acting on the caisson shaft and base, as follows:

- The distributed lateral springs k_x and dashpots c_x are associated with the horizontal soil reaction on the circumference (shaft) of the caisson.

- The distributed rotational springs k_θ and dashpots c_θ are associated with the moment produced by the vertical shear tractions on the circumference (shaft) of the caisson.
- The resultant base shear translational spring K_h and dashpot C_h associated with the horizontal shearing force on the base of the caisson.
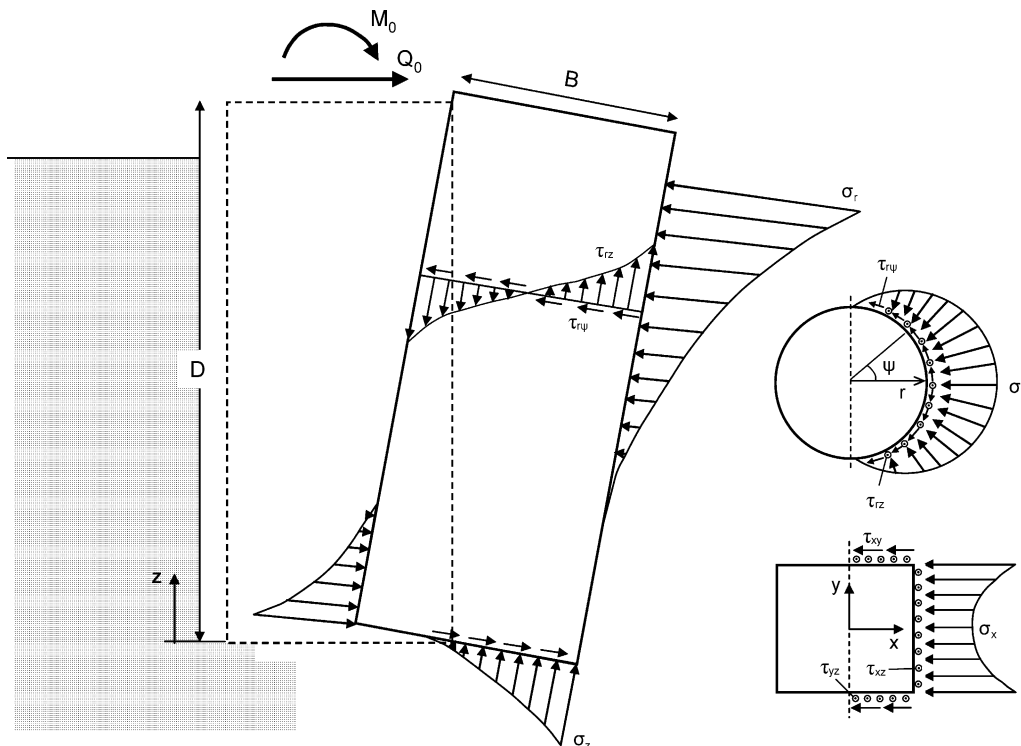

Fig. 2. Stresses at caisson–soil interface with circular, or square plan shape.
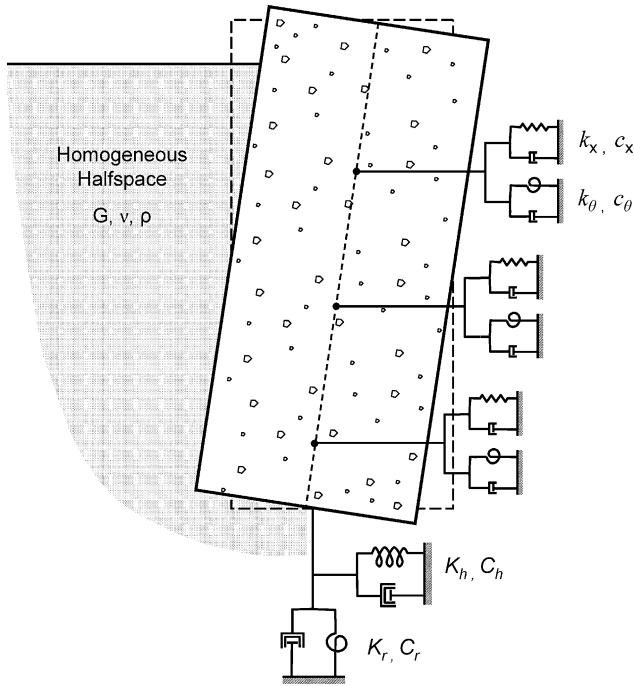
Fig. 3. The four-types of springs and dashpots for the analysis of inertially and kinematically loaded caissons.

- The resultant base rotational spring K_r and dashpot C_r associated with the moment produced by normal pressures on the base of the caisson.

The dashpot coefficients express the soil 'viscous' resistance that stems from both radiation of wave energy away from the caisson wall and hysteretic dissipation of energy in the soil. The proposed Winkler spring model is illustrated schematically in Fig. 3.

3. Lateral response of caisson: equations and parameters

The problem studied herein is that of circular, square, or rectangular in plan caisson embedded in homogeneous elastic soil over a deformable bedrock, and subjected to lateral dynamic excitation at its top: $Q_0(t)$ and $M_0(t)$ (Fig. 4). According to this figure the positive rotation and overturning moment are clockwise. The caisson is a rigid block of mass m, and mass moment of inertia about the center of gravity J_c. The depth of embedment of the caisson is D while the height of the sidewall that is in contact with the surrounding soil is d. The Winkler four-spring model described in the previous section is used for simulating the soil–caisson interaction. Dynamic equilibrium of the shear forces with respect to the base of the caisson gives

$$Q_0 - m\ddot{u}_c - P_x - Q_b = 0 \qquad (1)$$

where $u_c = u_c(t)$ is the displacement of the caisson at its center of gravity, given by

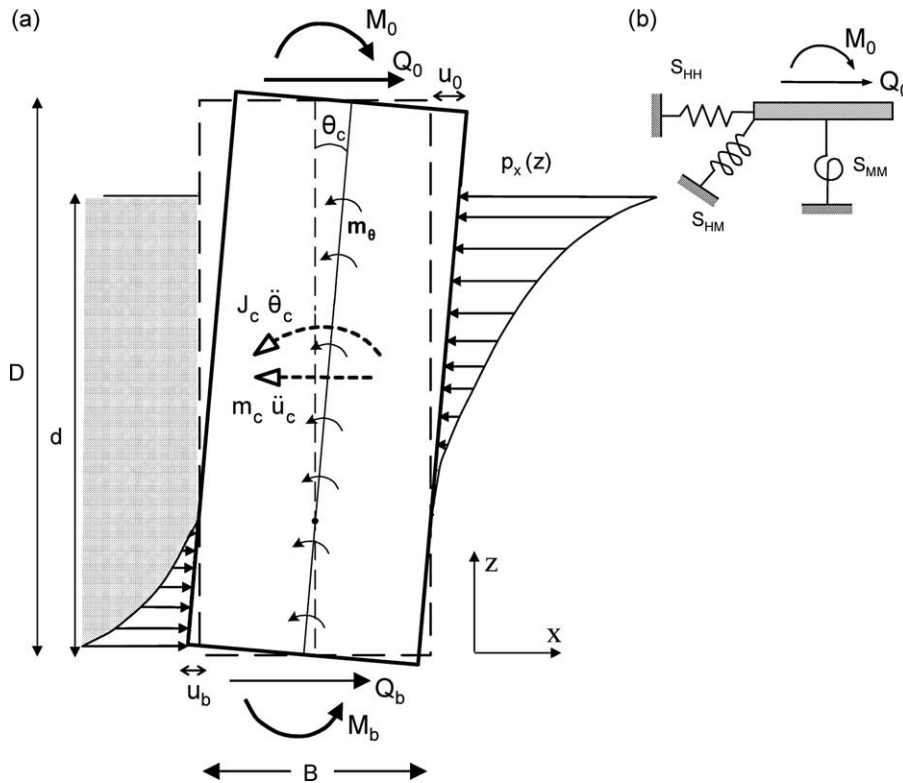$$u_c = u_b + \theta_c \frac{D}{2} \qquad (2)$$

Fig. 4. (a) Elastic response of a caisson subjected to lateral dynamic loading M_0, Q_0 at its top. (b) Schematic definition of the global stiffnesses (i.e. at the top of the caisson) in lateral translation (S_{HH}), rotation (S_{MM}) and cross-coupling of the translation and rotation (S_{HM}). The associated dashpot terms are not shown for the sake of clarity of the figure.

where $u_b = u_b(t)$ is the displacement of the caisson base, and $\theta_c = \theta_c(t)$ the rotation angle of the caisson. $P_x = P_x(t)$ is the resultant sidewall horizontal resistance due to the lateral soil reaction (Fig. 2),

$$P_x = \int_0^d p_x(z,t)\mathrm{d}z = \int_0^d [k_x(z)u(z,t) + c_x(z)\dot{u}(z,t)]\mathrm{d}z \qquad (3)$$

where z is the spatial coordinate starting from the base of the caisson, u is the displacement of the caisson at the location z determined as

$$u = u_b + \theta_c z \qquad (4)$$

and Q_b the shear resistance at the base of the caisson given by

$$Q_b = K_h u_b + C_h \dot{u}_b \qquad (5)$$

Dynamic moment equilibrium with respect to the base of the caisson gives

$$M_0 + Q_0 D - J_c \ddot{\theta}_c - m\frac{D}{2}\ddot{u}_c - M_x - M_\theta - M_b = 0 \qquad (6)$$

where $M_x = M_x(z,t)$ and $M_\theta = M_\theta(z,t)$ are the sidewall resisting moments arising from the horizontal soil reaction p_x and the vertical shear stresses τ_{xz} or τ_{rz}, respectively, on the caisson periphery. M_x is expressed as

$$M_x = \int_0^d p_x(z,t)z\,\mathrm{d}z = \int_0^d [k_x(z)u(z,t) + c_x(z)\dot{u}(z,t)]z\,\mathrm{d}z \qquad (7)$$

and M_θ as

$$M_\theta = \int_0^d m_\theta(z,t)\mathrm{d}z = \int_0^d [k_\theta(z)\theta_c(t) + c_\theta(z)\dot{\theta}_c(t)]\mathrm{d}z \qquad (8)$$

M_b is the resultant resisting moment at the base of the caisson

$$M_b = K_r\theta_c + C_r\dot{\theta}_c \qquad (9)$$

Eqs. (1) and (6) can be rewritten in a matrix form as

$$\mathbf{M_b}\begin{Bmatrix}\ddot{u}_b \\ \ddot{\theta}_b\end{Bmatrix} + \mathbf{C_b}\begin{Bmatrix}\dot{u}_b \\ \dot{\theta}_b\end{Bmatrix} + \mathbf{K_b}\begin{Bmatrix}u_b \\ \theta_b\end{Bmatrix} = \mathbf{P_b} \qquad (10)$$

where the mass matrix

$$\mathbf{M_b} = \begin{bmatrix} m & m\dfrac{D}{2} \\[2mm] m\dfrac{D}{2} & J_c + m\dfrac{D^2}{4} \end{bmatrix} \qquad (11)$$

the stiffness matrix

$$\mathbf{K_b} = \begin{bmatrix} K_{hh} & K_{hr} \\ K_{hr} & K_{rr} \end{bmatrix}$$

$$= \begin{bmatrix} K_h + \displaystyle\int_0^d k_x(z)\mathrm{d}z & \displaystyle\int_0^d k_x(z)z\,\mathrm{d}z \\[4mm] \displaystyle\int_0^d k_x(z)z\,\mathrm{d}z & K_r + \displaystyle\int_0^d k_x(z)z^2\,\mathrm{d}z + \displaystyle\int_0^d k_\theta(z)\mathrm{d}z \end{bmatrix} \qquad (12)$$

$$\mathbf{C_b} = \begin{bmatrix} C_{hh} & C_{hr} \\ C_{hr} & C_{rr} \end{bmatrix}$$

$$= \begin{bmatrix} C_h + \displaystyle\int_0^d c_x(z)\mathrm{d}z & \displaystyle\int_0^d c_x(z)z\,\mathrm{d}z \\[4mm] \displaystyle\int_0^d c_x(z)z\,\mathrm{d}z & C_r + \displaystyle\int_0^d c_x(z)z^2\,\mathrm{d}z + \displaystyle\int_0^d c_\theta(z)\mathrm{d}z \end{bmatrix} \qquad (13)$$

and the damping matrix (due to both radiation and hysteretic dissipation in the soil). The external force vector $\mathbf{P_b}$ is

$$\mathbf{P_b} = \begin{Bmatrix} Q_0 \\ M_0 + Q_0 D \end{Bmatrix} \qquad (14)$$

In the frequency domain, the complex stiffness matrix of the caisson is calculated as

$$\tilde{\mathbf{K}}_b = \mathbf{K_b} + i\omega\mathbf{C_b} \qquad (15)$$

which using Eqs. (12), (13), and (15), reduces to

$$\tilde{\mathbf{K}}_b = \begin{bmatrix} \tilde{K}_h + \tilde{k}_x D & \tilde{k}_x\dfrac{D^2}{2} \\[3mm] \tilde{k}_x\dfrac{D^2}{2} & \tilde{K}_r + \tilde{k}_\theta D + \dfrac{1}{3}\tilde{k}_x D^3 \end{bmatrix} \qquad (16)$$

The dynamic impedance matrix, $\bar{S}$, referred to the top of the caisson is readily obtained by a coordinate transformation of Eq. (15)

$$\bar{S} = \begin{bmatrix} \tilde{S}_{HH} & \tilde{S}_{MH} \\ \tilde{S}_{MH} & \tilde{S}_{MM} \end{bmatrix}$$

$$= \begin{bmatrix} \tilde{K}_{hh} & \tilde{K}_{hr} - D\tilde{K}_{hh} \\ \tilde{K}_{hr} - D\tilde{K}_{hh} & \tilde{K}_{rr} - 2D\tilde{K}_{hr} + D^2\tilde{K}_{hh} \end{bmatrix} \qquad (17)$$

The meaning of the impedances $\bar{S}_{ij}$ is sketched in the insert of Fig. 3. The reliability of the proposed Winkler-type model depends on the proper choice of the dynamic spring and dashpot coefficients. These coefficients are frequency dependent and are functions of both caisson geometry and soil stiffness. In the following, a simple methodology for the calibration of

the parameters of the four-spring model is developed, utilising published results for embedded foundation.

4. Calibration of the spring and dashpot coefficients

Gazetas and Tassoulas [15,16] and Fotopoulou et al. [17] studied the problem of the lateral oscillation of arbitrarily shaped rigid foundations embedded in a homogeneous elastic halfspace, as depicted in Fig. 5. Based on some simple physical models calibrated with results of rigorous boundary-element and finite-element elastodynamic formulations, as well as data from the literature, they developed closed-form expressions for the dynamic impedances of such foundations [18,21]. For an arbitrarily shaped foundation in plan view, circumscribed by a rectangle of width B and length L ($L > B$), they express the dynamic impedances, with respect to the center of the base mat, in the form

$$\tilde{K}_{emb} = K_{emb}\chi_{emb}(\omega) + i\omega C(\omega) \tag{18}$$

where K_{emb} is the static stiffness, and $\chi_{emb}(\omega)$ the dynamic stiffness coefficient. $C(\omega)$ is the frequency-dependent (radiation and material) damping coefficient. The parameters that enter in the computation of stiffness and damping in Eq. (18), are

- G_s, E_s, V_s, V_a, ν: shear modulus, modulus of elasticity, shear wave velocity, apparent analog velocity, and Poisson's ratio
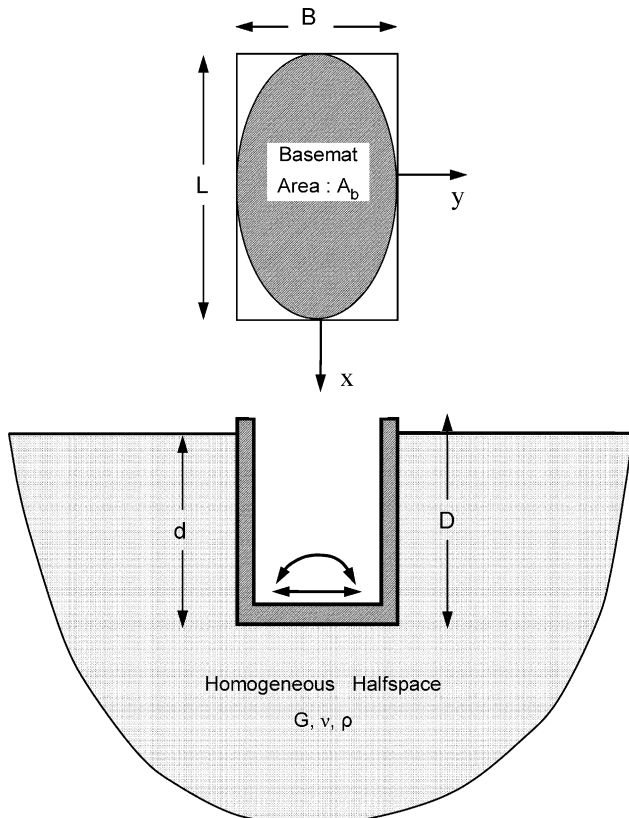

Fig. 5. Geometry of a rigid foundation arbitrarily-shaped in plan embedded in a homogeneous elastic halfspace.

of the soil. Of course, only(any) two of them are enough to determine all other.

- B, L, D and d: width, length, depth of embedment, and height of the sidewall that is in contact with the surrounding soil.
- A_b, I_b and h: area, moment of inertia, and distance of the centroid of the effective sidewall from the ground surface.
- A_w: total area of the actual sidewall–soil contact surface (perimeter times D).
- $A_{w,s}$ and $A_{w,ce}$: refer to horizontal oscillations and represent the sum of the projections of all the sidewall areas in direction parallel ($A_{w,s}$) and perpendicular ($A_{w,ce}$) to loading, subjected to shear (s) and compression–extension (ce) type of soil reaction, respectively.
- J_{ws} and I_{wce}: the sum of the polar moments of inertia about the off-plane axis of rotation of all surfaces actually shearing the soil, and the sum of moments of inertia of all surfaces actually compressing the soil about their base axes parallel to the axis of rotation.
- Δ_i: The distance of surface $A_{wce,i}$ from the x axis.

Gazetas and workers developed the following formulae for stiffness and damping in the longitudinal x-axis of a orthogonal or cylindrical caisson

$$K_{HH}(\omega)$$

$$\approx K_H \left(1 + 0.15\sqrt{\frac{2D}{B}}\right)\left[1 + 0.52\left(\frac{8hA_w}{BL^2}\right)^{0.4}\right]\chi_{emb}(\omega) \tag{19}$$

where K_H is the static horizontal stiffness of the caisson base [15], and χ_{emb} is a dynamic stiffness coefficient presented in chart form [15,18] in terms of D/B and d/B as a function of the dimensionless parameter a_0 ($= \omega B/2V_s$). In the case of a fully embedded caisson, curve fitting gives χ_{emb} in the form

$$\chi_{emb} \approx 1$$
$$+ a_0\left(\frac{D}{B}\right)\left\{\left[0.08 - 0.0074\left(\frac{D}{B}\right)\right]a_0^2\right. \tag{20}$$
$$\left. - \left[0.31 - 0.0416\left(\frac{D}{B}\right)\right]a_0 - 0.0442\left(\frac{D}{B}\right) + 0.14\right\}$$

The horizontal dashpot coefficient is

$$C_{HH}(\omega) = C_H(\omega) + \rho V_s A_{ws} + \rho V_a A_{wce} \tag{21}$$

where

$$C_H(\omega) = \rho V_s A_b c_{sur}(\omega) \tag{22}$$

where $C_H(\omega)$ is the damping coefficient of the caisson base [16], taken as that of a surface foundation on halfspace. The coupled swaying-rocking complex impedance is approximated by

$$\tilde{K}_{HM} \approx \frac{1}{3}d\tilde{K}_{HH} \tag{23}$$

The dynamic rocking stiffness is equal to

$$K_{MM}(\omega) = K_M(\omega)\left\{1 + 0.92\left(\frac{2d}{L}\right)^{0.6}\left[1.5\right.\right.$$
$$\left.\left. + \left(\frac{2d}{L}\right)^{1.9}\left(\frac{d}{D}\right)^{-0.6}\right]\right\}(1 - 0.30a_0) \qquad (24)$$

where K_M is the static rocking stiffness of the caisson base [18], taken as that of a surface foundation on halfspace. The radiation dashpot constant in rocking oscillation is expressed as

$$C_{MM}(\omega) = C_M(\omega) + \rho V_{La}I_{wce}c_1(\omega)$$
$$+ \rho V_s\left[J_{ws} + \sum_i\left(A_{wcei}\Delta_i^2\right)\right]c_1(\omega) \qquad (25)$$

where $C_M(\omega)$ is the dashpot of the caisson base [17]. The dynamic dashpot coefficient c_1 is given by

$$c_1 \approx 0.25 + 0.65\sqrt{a_0}\left(\frac{d}{D}\right)^{-a_0/2}\left(\frac{2D}{B}\right)^{-0.25} \qquad (26)$$

Thus, the complex dynamic impedance matrix of the caisson referring to the base has been calculated as

$$\tilde{\mathbf{K}}_{emb} = \begin{bmatrix} \tilde{K}_{HH} & \tilde{K}_{HM} \\ \tilde{K}_{HM} & \tilde{K}_{MM} \end{bmatrix} \qquad (27)$$

There is a number of ways to determine the complex spring stiffnesses functions $\tilde{k}_k$ and $\tilde{k}_\theta$ of the 'equivalent' Winkler model. The simplest way that we follow here is to equate the diagonal terms in the matrices of Eqs. (16) and (27). A check is then necessary to ensure that the resulting off-diagonal cross-term K_{HM} in Eq. (33) is at least reasonably similar with the respective term in Eq. (17). We thus derive

$$\tilde{k}_x = k_x + i\omega C_x = \frac{1}{D}(\tilde{K}_{HH} - \tilde{K}_h) \qquad (28)$$

and

$$\tilde{k}_\theta = k_\theta + i\omega C_\theta$$
$$= \frac{1}{D}\left(\tilde{K}_{MM} - \tilde{K}_r + \frac{1}{3}D^2\tilde{K}_h - \frac{1}{3}\tilde{K}_{HH}D^2\right) \qquad (29)$$

These are the general expressions from which the distributed springs and dashpots of the model can be derived (easily, even if not always in closed form) for any shape in plan of the caisson. For instance, for the particular cases of greatest interest, the square and circular plan shapes, and static lateral loading the above equations yield the following distributed springs
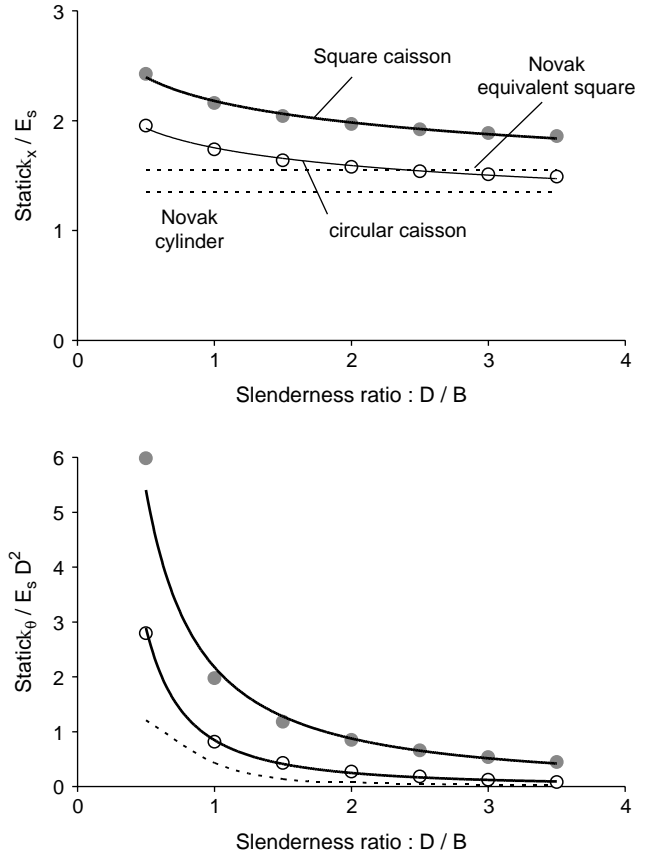

Fig. 6. Comparison of the translational (top) and rotational (bottom) static spring stiffnesses, calculated with the simplified Eqs. (30) and (31) (solid lines) and the exact Eqs. (28) and (29) (circles). Novak's [24] solution is plotted with dotted lines.

- *Square caisson*

$$k_x \approx 2.18\left(\frac{D}{B}\right)^{-0.13}E_s \quad \text{and} \quad k_\theta \approx 2.17\left(\frac{D}{B}\right)^{-1.31}E_sD^2 \qquad (30)$$

- *Circular caisson*

$$k_x \approx 1.75\left(\frac{D}{B}\right)^{-0.13}E_s \quad \text{and} \quad k_\theta \approx 0.85\left(\frac{D}{B}\right)^{-1.71}E_sD^2 \qquad (31)$$

Fig. 6 compares the static spring stiffnesses derived from the approximated relations of Eqs. (30) and (31), with their exact values calculated from Eqs. (28) and (29). It is interesting to note that for a slenderness ratio $D/B \approx 10$, Eq. (31) for the cylindrical caisson simplify to

$$k_x \approx 1.2E_s \quad \text{and} \quad k_\theta \approx 0 \qquad (32)$$

which are reminiscent of the spring moduli used for laterally loaded piles, e.g. Ref. [22]. Novak's spring stiffnesses [24] for $a_0 = 0.3$ are also plotted in Fig. 6. Novak's solution underestimates slightly the horizontal spring stiffness at small D/B values, but quite severely the rotational one. This was anticipated since Novak's springs are derived for a 2D horizontal slice of the caisson and surrounding soil
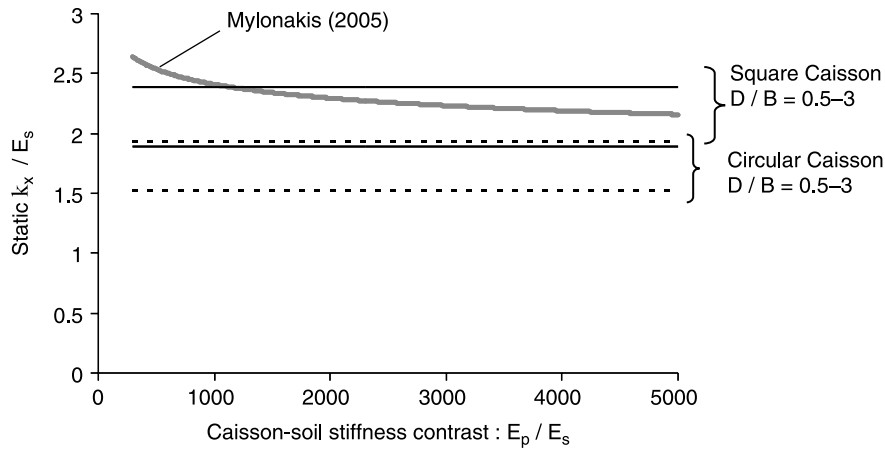
Fig. 7. Comparison of the translational static spring stiffness, calculated with the simplified Eqs. (30) and (31) (dotted black lines) and Mylonakis' (2005) solution (grey solid line) for a flexible fixed-head and infinitely-long circular caisson, and for Poisson's ratio of the soil $\nu_s = 0.3$.

(plane strain condition) and do not account for the 3D geometry of caisson foundations.

Fig. 7 compares the static spring stiffness derived from the approximate relations of Eq. (30) for a square caisson and Eq. (31) for a circular caisson, with the Mylonakis' [23] solution for a flexible fixed-head and infinitely-long circular caisson. The comparison, however, is not straightforward given that Mylonakis' solution is a function of the caisson–soil stiffness contrast, E_p/E_s, while Eqs. (30) and (31) are valid only for rigid caissons and depend only on the slenderness ratio D/B. The comparisons are quite satisfactory, especially if one considers the different assumptions adopted in the two solutions.
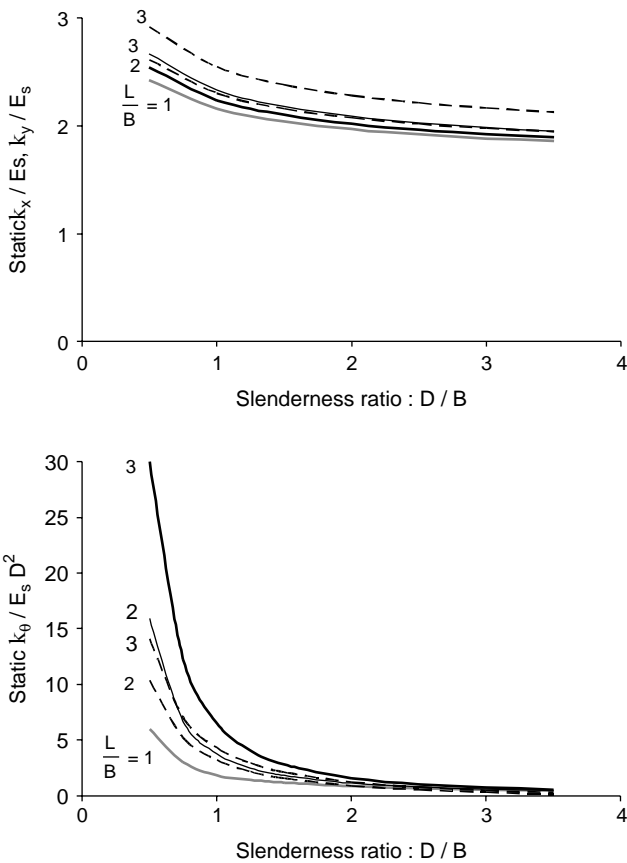
Fig. 8. Static spring stiffnesses, translational (top) and rotational (bottom), for a rectangular caisson for length to width ratio $L/B = 1$, 2 and 3. The stiffnesses in the longitudinal direction (x) are plotted with solid lines, and those in the lateral direction (y) with dotted lines.
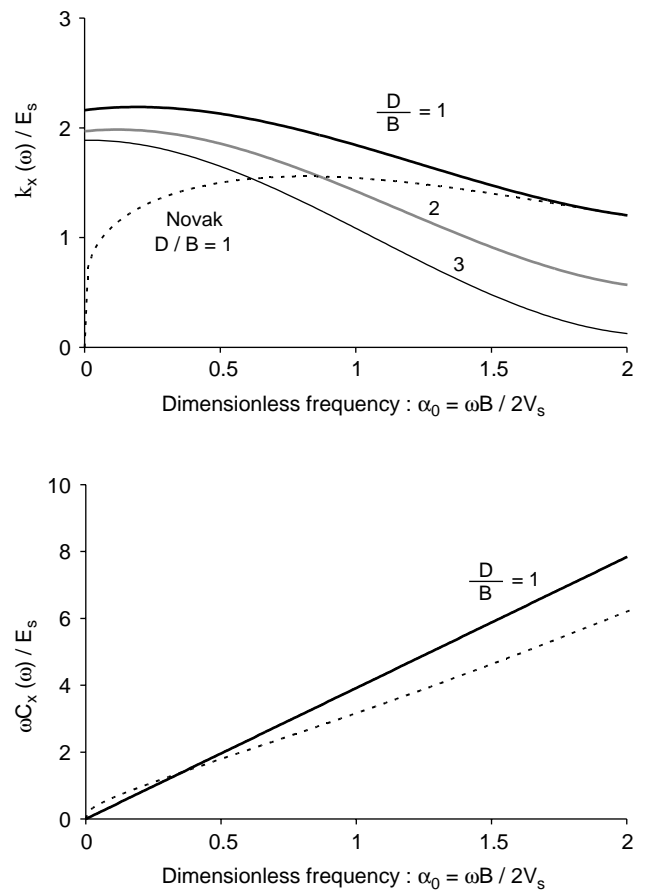

Fig. 9. Normalized dynamic translational spring stiffness (top), and dashpot coefficients (bottom) for a square caisson with slenderness ratio $D/B = 1$, 2 and 3, computed with Eq. (28). Novak's [24] spring and dashpot coefficient for a cylindrical caisson with slenderness ratio $D/B = 1$ are plotted with dotted lines for comparison.

Fig. 8 illustrates the dependence on the slenderness ratio D/B of the static spring stiffnesses derived from Eqs. (28) and (29), for 'aspect' (length to width) ratios $L/B = 1$, 2, and 3. While the translational stiffness is practically insensitive to variations in either the slenderness or the aspect ratios, the rotational stiffness is strongly affected. Results for elliptical foundation plan could be derived using the expression presented recently by Mylonakis et al. [21].

5. Parametric study of the inertial caisson response

This chapter presents the results of a parametric study aimed at investigating the influence of several key parameters on the lateral dynamic response of fully-embedded square-shaped caisson foundations.

Figs. 9 and 10 compare the normalized translational and the rotational stiffnesses of the distributed (local) soil springs as functions of the dimensionless frequency a_0. Three different slenderness ratios ($D/B = 1$, 2, and 3) are examined. Note that as the slenderness ratio increases, the dynamic stiffnesses (translational, normalized by E_s and rotational normalized by $E_s D^2$) decrease. This reveals that in the limit of extremely high slenderness the vertical shear resistance mechanism along the
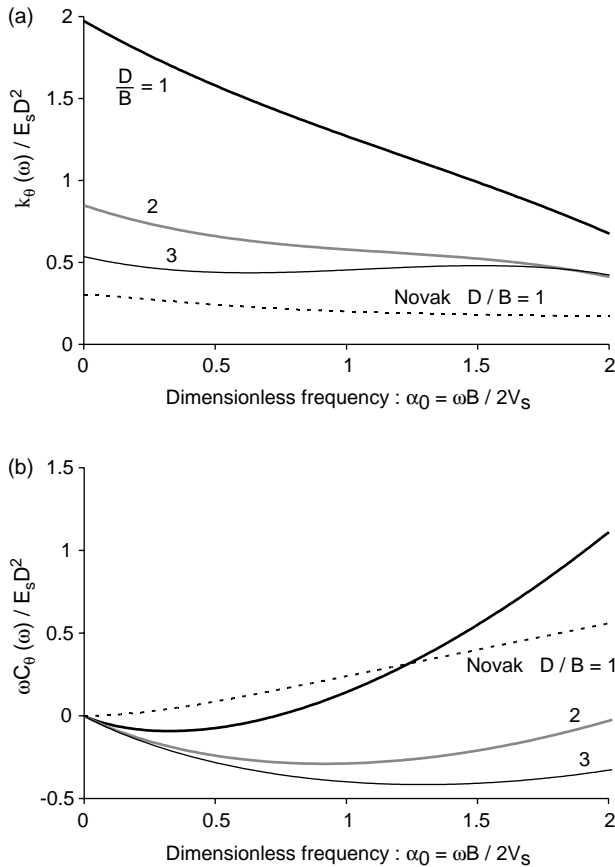
(a)

Fig. 10. Normalized coefficients (a) k_θ and (b) c_θ of dynamic rotational spring and dashpot (distributed along the depth) for square caissons with slenderness ratios $D/B = 1$, 2 and 3, computed with Eq. (29). The spring and dashpot curves computed using the Novak et al. [24] approximation for a cylindrical caisson with slenderness ratio $D/B = 1$ are plotted with dotted lines.
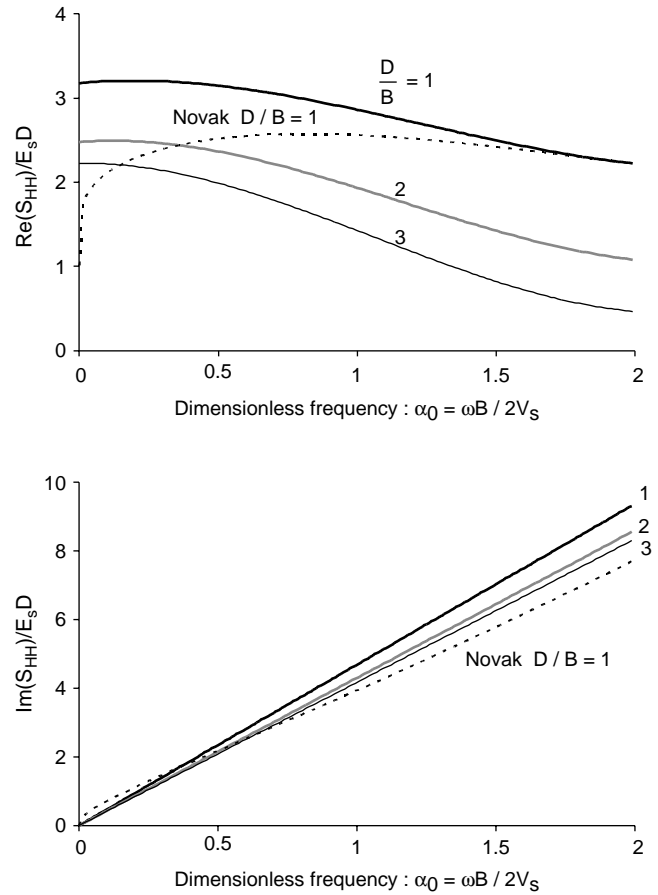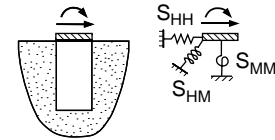
Fig. 11. Normalized real and imaginary part of the resultant swaying stiffness atop a square caisson, for slenderness ratios $D/B = 1$, 2 and 3. Solution for $D/B = 1$ using Novak's method gives the dotted curves.

circumference vanishes and the caisson behavior approaches that of a pile. Novak's springs [24] for $D/B = 1$ are also plotted in Figs. 9 and 10. It is interesting to note that the static translational stiffness derived from Novak's plane strain solution is equal to zero.

Figs. 11–13 illustrate the normalized real and imaginary parts of the complex global stiffnesses (namely the swaying, rocking, and cross swaying–rocking components) atop of the caisson utilizing the distributed springs from Eqs. (28) to (29), and those proposed by Novak. Notice that the dynamic stiffnesses are decreasing functions of the dimensionless frequency a_0. But the normalized imaginary parts increase almost linearly with frequency, which would lead to the filtering-off of the high-frequency components of a seismic motion.

Fig. 14 shows the magnitude of the dynamic to static displacement and rotation ratio, respectively, atop the caisson, for unit shear force ($Q_0 = 1$) and zero bending moment ($M_0 = 0$). The ratios are plotted as functions of the dimensionless
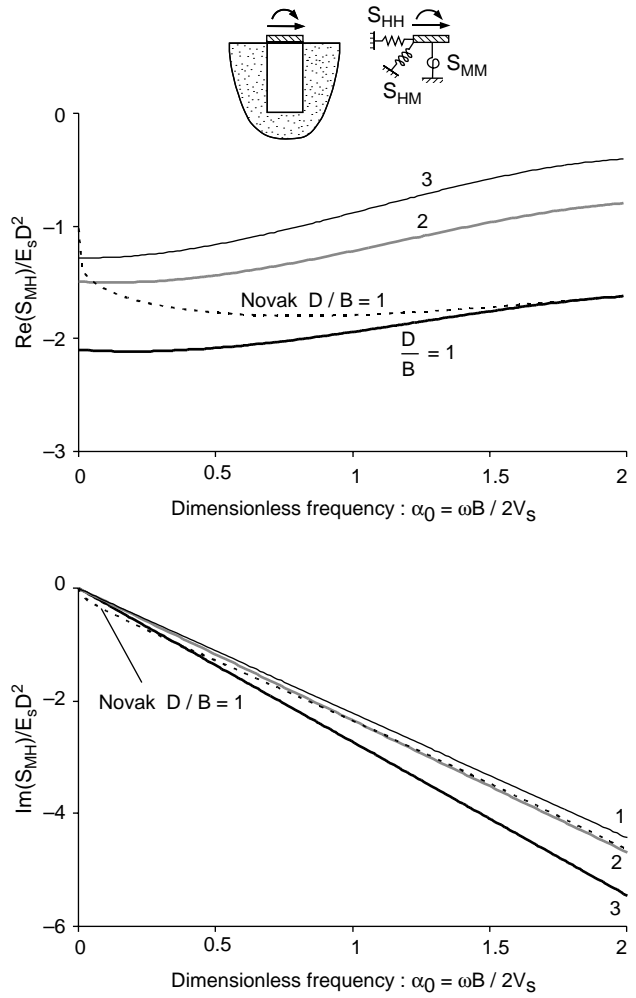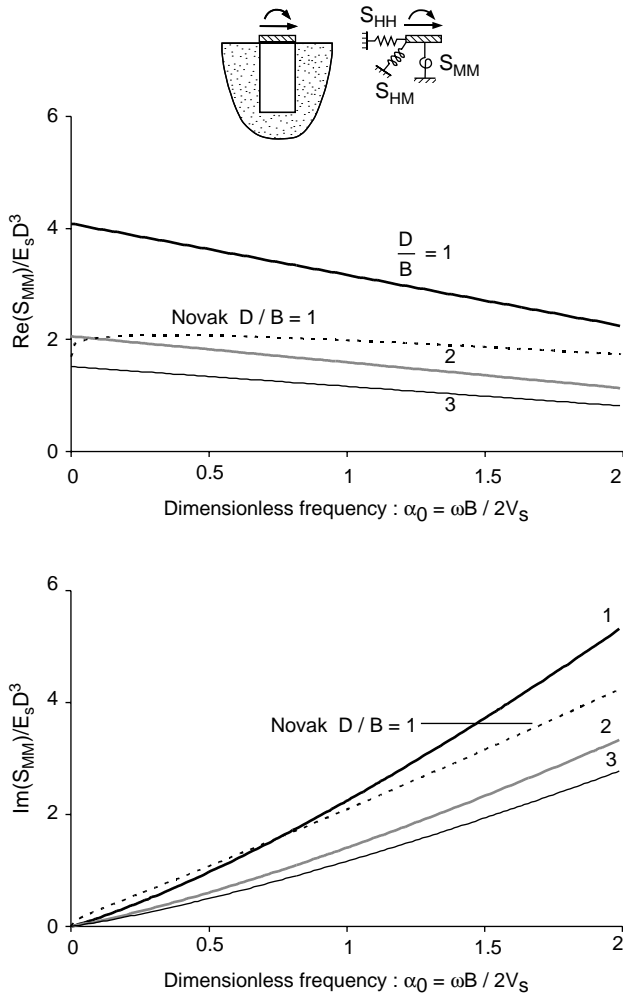
Fig. 12. Normalized real and imaginary part of the resultant rocking stiffness atop a square caisson, for slenderness ratios $D/B = 1$, 2 and 3. Solution for $D/B = 1$ using Novak's method gives the dotted curves.

Fig. 13. Normalized real and imaginary part of the resultant cross swaying–rocking stiffness atop a square caisson, for slenderness ratios $D/B = 1$, 2 and 3. Solution for $D/B = 1$ using Novak's method gives the dotted curves.

frequency a_0 for three values of slenderness ratio D/B. The hysteretic damping ratio ξ is equal to zero. Observe that due to the huge radiation damping the system exhibits no resonance phenomena. For frequencies above the first fundamental frequency of the caisson the motion vanishes exponentially.

Fig. 15 illustrates the normalized dynamic displacement and rotation atop the caisson, as a function of the dimensionless frequency a_0 for selected values of normalized loading ratio $M_0/Q_0 D$. The curves correspond to a slenderness ratio of $D/B = 2$. Small values of the loading ratio $M_0/Q_0 D$ correspond to short superstructure systems (such as short bridge piers), while larger values are representative of tall systems. We conclude that while the normalized displacement is an increasing function of the loading ratio, the normalized rotation remains, surprisingly, insensitive.

To interpret this paradox, we investigate the influence of the existence of a cut-off frequency for radiation damping on the response of the caisson. Fig. 16 plots the same results with those of Fig. 15 except that the radiation damping is spuriously reduced to merely 10% of its actual value. This is

representative of a foundation response when the fundamental period of its supported superstructure is larger than the first natural period of the soil. The two eigenfrequencies of the caisson–soil system can be easily observed in this figure. The first one ($a_0 \approx 1.30$) corresponds to the translational mode, and the second ($a_0 \approx 2.25$) to the rotational mode. For a loading ratio $M_0/Q_0 D = 0$, the maximum normalized displacement occurs at the first eigenfrequency of the caisson–soil system. Increasing the loading ratio the contribution of the second eigenfrequency grows up, and finally dominates the response for loading ratios greater than five. On the other hand, the peak normalized rotation is controlled by the second eigenfrequency; the contribution of the first eigenfrequency to the rotational oscillation is negligible and decreases with increasing loading ratio. But the second fundamental frequency of the caisson–soil system corresponds to high frequencies where the radiation damping in a homogeneous halfspace is huge, leading eventually to normalized rotation being less affected by variations in the loading ratio.
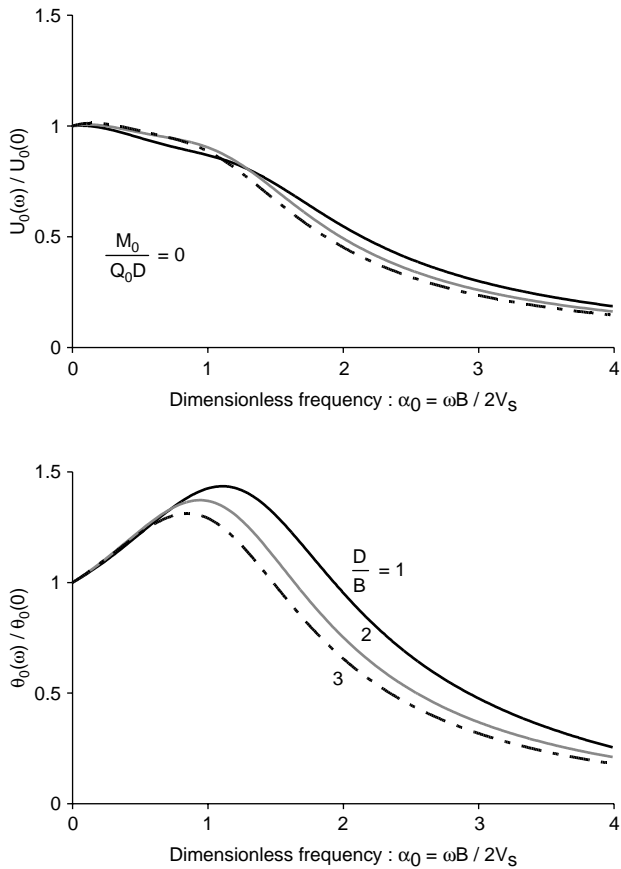
Fig. 14. Magnitude of the dynamic to static ratios of displacement (top) and rotation (bottom) atop a square caisson. Slenderness ratios $D/B = 1$, 2 and 3. Loading ratio $M_0/Q_0D = 0$.
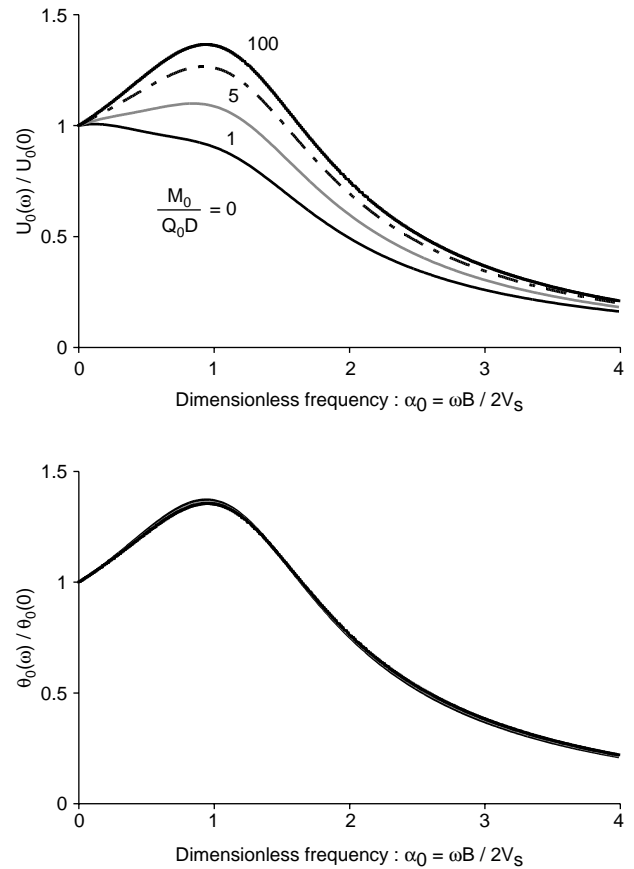
Fig. 15. Magnitude of the dynamic to static ratios of displacement (top) and rotation (bottom) atop a square caisson. Loading ratios $M_0/Q_0D = 0$, 1, 5, 100, and slenderness ratio $D/B = 2$.

Fig. 17 investigates the influence of hysteretic damping on the normalized displacements of a caisson ($\xi = 0$ and 10%, respectively). Plots are given for a slenderness ratio $D/B = 2$, and for three values of the loading ratio. The full radiation damping of the caisson has been taken into account. Observe that the influence of the hysteretic damping on the response of the caisson is small and could be ignored in design without any remarkable loss.

6. Comparison with results of 3D-finite element analysis

As an attempt to evaluate the accuracy of the model, a comparison is performed with results from finite element analysis. The problem studied is a rigid circular caisson of height $D = 6$ m and diameter $B = 3$ m ($D/B = 2$), embedded in homogeneous elastic soil stratum. Young's modulus, Poisson's ratio, mass density, and hysteretic damping of the soil are constant with depth: $E_s = 100$ MPa, $\nu_s = 0.3$, $\rho_s = 2$ mg/m^3, and $\xi = 0\%$. A detailed numerical model of the caisson and the surrounding soil is developed with the code ABAQUS. The finite element mesh used in the analysis is depicted in Fig. 18. Both the caisson and the soil are modeled with 3D elements. The far field is represented with infinite elements ensuring that the displacements vanish 'at infinity'. The soil stratum reaches

10 m deeper than the caisson base, thus having a negligible influence on its response.

Steady-state analyses were performed to compute the magnitude of the dynamic to static ratios of displacement (a) and rotation (b) atop the caisson. The normalized loading ratios M_0/Q_0D are 0 and 1.67. The results of the finite element and the Winkler method are compared in Fig. 19. The agreement is quite good, with the proposed method predicting slightly larger values than those of the finite element model.

7. Kinematic response of caisson

While long-pile foundations could simply follow more-or-less the seismic motion of the ground, in many cases, caissons (characterized by considerable rigidity) modify the soil deformation and generate additional soil strains in their vicinity. As a result, the incident seismic waves are scattered and the seismic excitation to which the caisson-foundation is effectively subjected to differs from that of the free field motion. This kinematic filtering effect is more pronounced at small slenderness ratios and high bending rigidity. Increasing frequency of the excitation, tends to increase the waviness of the soil response and thereby increases the filtering effect.
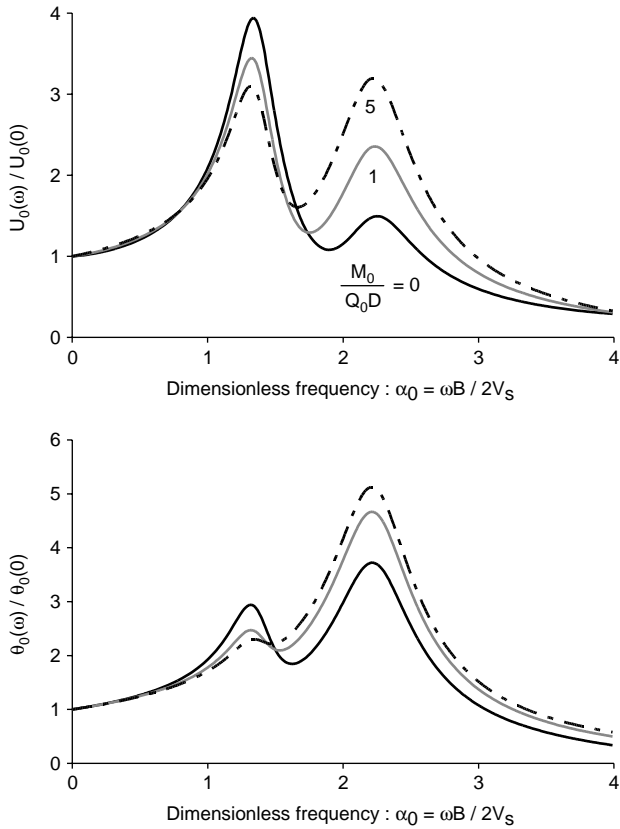
Fig. 16. Magnitude of the dynamic to static displacement (top) and rotation (bottom) ratio atop a square caisson for loading ratios $M_0/Q_0D=0$, 1, 5, and for slenderness ratio $D/B=2$. The radiation damping of the caisson is reduced to 10% of its actual value.

The problem studied herein is that of a rectangular or circular in-plan caisson embedded in a single layered elastic soil over a flexible bedrock, and subjected to kinematic loading due to vertical shear wave propagation. Solution is carried out in two steps: (a) the free-field soil response (without the presence of the caisson) is first calculated, and (b) this free-field
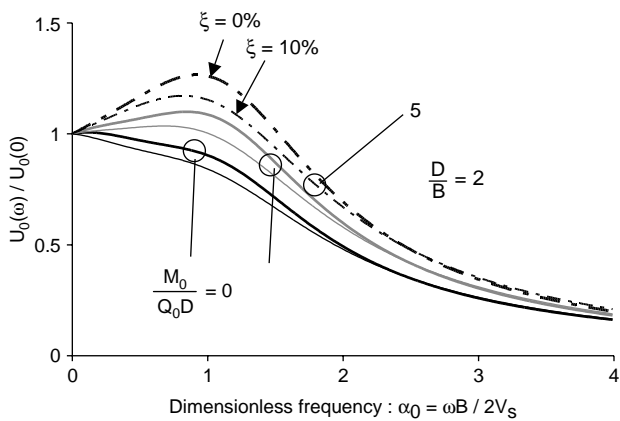

Fig. 17. Comparison of the normalized dynamic displacement atop a square-shaped caisson for hysteretic damping ratios equal to $\xi=0$ and 10%, respectively.
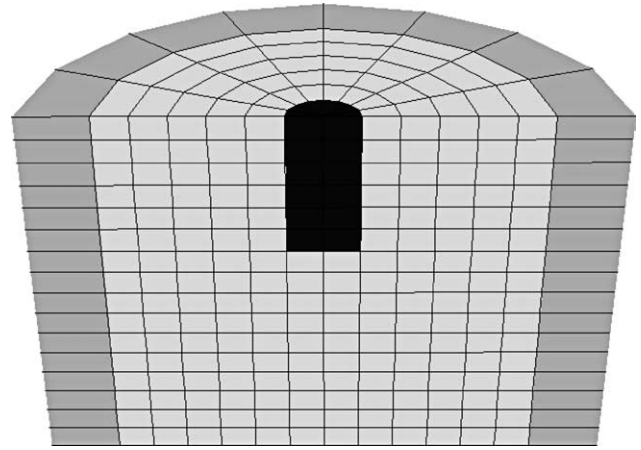

Fig. 18. The finite element mesh used in the analysis. The caisson elements are shown with deep grey colour, the surrounding soil elements with soft grey, and the infinite elements with mid grey colour.

motion is then imposed at the supports of the caisson springs and dashpots. The method of analysis is schematically illustrated in Fig. 20.

Equations of motion with respect to the base of the caisson are derived from Eq. (10) by replacing the vector of effective
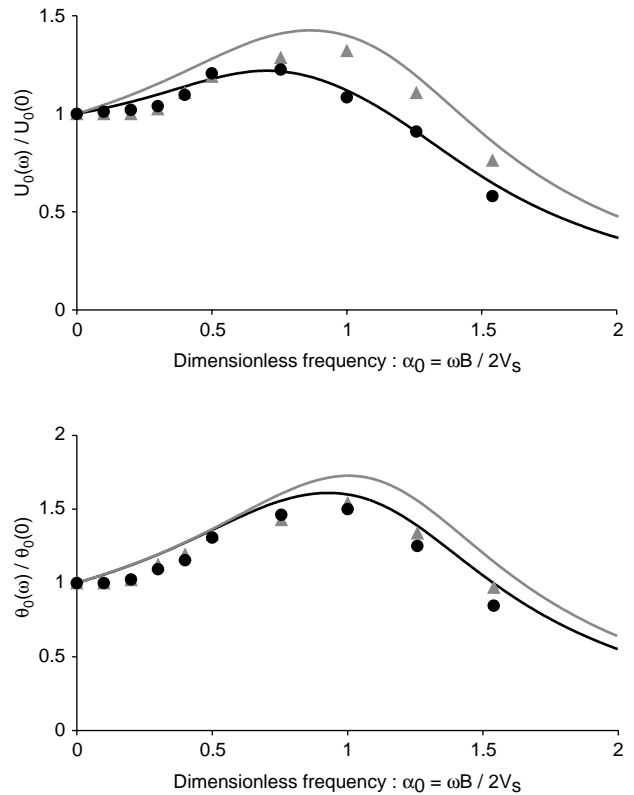

Fig. 19. Magnitude of the dynamic to static ratios of displacement (top) and rotation (bottom) atop the cylindrical caisson ($D=6$ m, $B=3$ m) of Fig. 18 for loading ratios $M_0/Q_0D=0$ (black lines and circles) and 1.67 (grey lines and triangles), computed with the proposed Winkler model (solid lines) and the finite element model (triangles and circles).
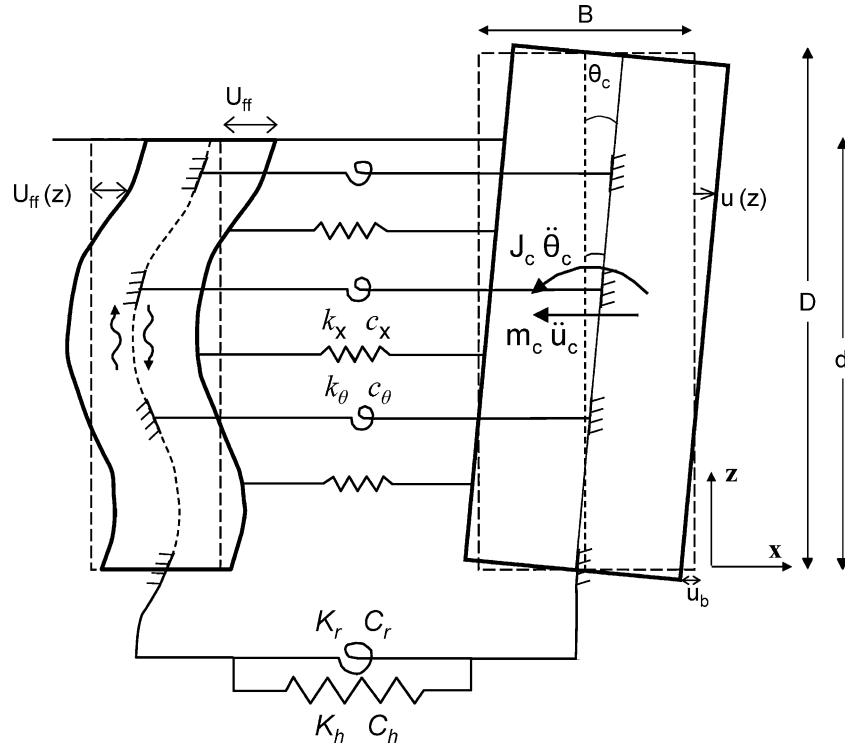
Fig. 20. Schematic illustration of the method of analysis of the response of a 'kinematically' loaded caisson: The free-field motion due to vertical shear waves (left) imposes horizontal displacement and rotation at the supports (i) of the distributed springs and dashpots (k_x, c_x; k_θ, c_θ) along the caisson height, and (ii) of the resultant springs and dashpots (K_h, C_h; K_r, C_r) of the base.

loading, $\mathbf{P_b}$, given in Eq. (14) with

$$\mathbf{P_b} = \left\{ \begin{array}{c} \displaystyle\int_0^d \tilde{k}_x(z) U_{ff}(z)\,dz + \tilde{K}_h U_{ff}(0) \\[2em] \displaystyle\int_0^d \tilde{k}_x(z) U_{ff}(z) z\,dz + \int_0^d \tilde{k}_\theta(z) U'_{ff}(z)\,dz + \tilde{K}_r U'_{ff}(0) \end{array} \right\} \quad (33)$$

where U_{ff} and U'_{ff} are the free-field displacement and its derivative with respect to z. Details on the derivation of Eq. (33) is given in Appendix A. For an elastic soil layer supported on a 'flexible' bedrock, U_{ff} is equal to [25]

$$U_{ff}(z) = U_g \frac{\exp[i\kappa(D-z)] + \exp[-i\kappa(D-z)]}{(1+\alpha)\exp(i\kappa D) + (1-\alpha)\exp(-i\kappa D)} \quad (34)$$

where U_g is the displacement amplitude at the base of the soil layer, κ is the complex wave number given by

$$\kappa = \frac{\omega}{V_s \sqrt{1+2i\xi_s}} \quad (35)$$

where α is the complex impedance ratio given by

$$\alpha = \frac{\rho_s V_s \sqrt{1+2i\xi_s}}{\rho_r V_r \sqrt{1+2i\xi_r}} \quad (36)$$

where subscript s refers to soil and r to rock.

Solution of Eqs. (10) and (33) can be solved in closed form for this case of homogeneous stratum. This solution is explored herein in the form of parametric study. To present the results of our analysis in a convenient form, the following dimensionless

parameters are defined:

$$\eta_{eff}(\omega) = \frac{u_0(\omega)}{U_{ff}(D,\omega)} \quad (37)$$

the 'effective' displacement ratio at the top of the caisson,

$$\theta_{eff}(\omega) = \frac{\theta_0(\omega)D}{U_{ff}(D,\omega)} \quad (38)$$

the 'effective' rotation ratio at the top of the caisson,

$$\mathcal{A}_{ff}(\omega) = U_{ff}(D,\omega)/U_{ff}(0,\omega) \quad (39)$$

the amplification ratio at the top of the caisson

$$\mathcal{A}_c(\omega) = u_0(\omega)/U_{ff}(0,\omega) \quad (40)$$

the amplification ratio at the surface of the soil profile, and

$$\beta_0 = \frac{\omega D}{V_s} \quad (41)$$

the dimensionless frequency with respect to the caisson height.

Fig. 21 compares the 'effective' top displacement and rotation ratios of a square-shaped caisson for three typical slenderness ratios ($D/B = 1$, 2, and 3), as functions of the dimensionless frequency β_0. The solution developed by the authors utilizing Novak's springs for $D/B = 1$, is also shown in this figure. The hysteretic damping in the surrounding soil is equal to $\xi = 20\%$; in the free-field soil equal to $\xi_s = 5\%$. The mass density of the caisson has been ignored. It is noted that both top displacement and rotation of the caisson attain negligibly small (or even zero) values at a discretely infinite
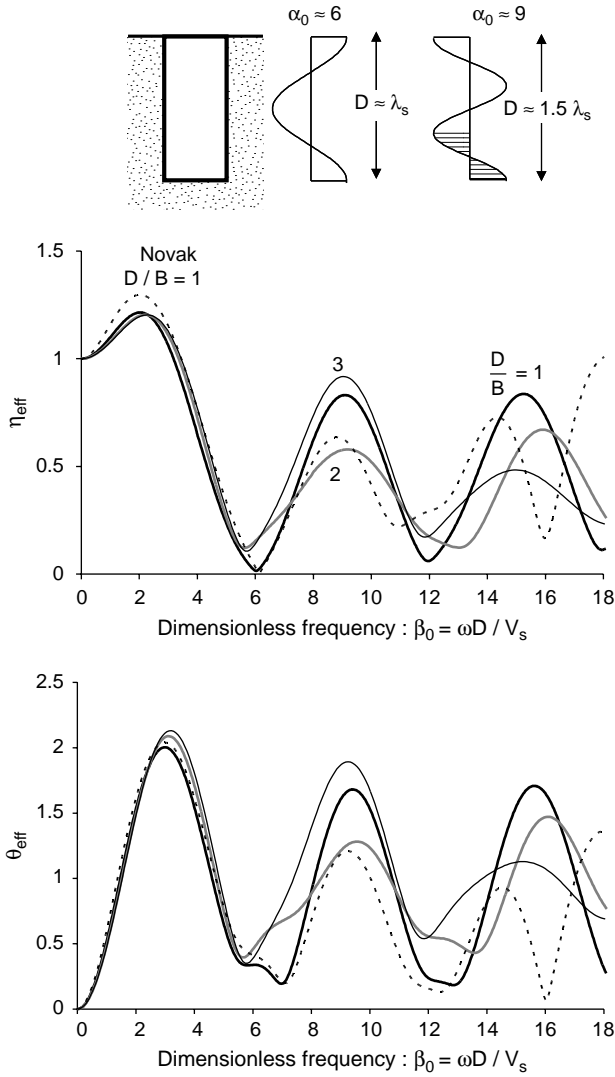
Fig. 21. Effective displacement (top) and rotation (bottom) ratios atop a square caisson for slenderness ratios $D/B = 1$, 2 and 3. The caisson is fully embedded in a homogeneous halfspace. The kinematic loading has been derived from the free-field response analysis of a soil column supported by a deformable bedrock of impedance ratio $\alpha = 0.07$. Solution for $D/B = 1$ derived by the authors using Novak's distributed springs and dashpots is plotted with dotted lines.

number of values of $\beta_0 = \beta_{0,n}$ which are multiple of about 6 (or slightly higher). This is understandable if we realize that a value

$$\beta_0 = \frac{\omega D}{V_s} \approx 2\pi \frac{D}{\lambda_s} \approx 6$$

implies that the wavelength λ_s of the free-field shear wave is about equal to the length D of the caisson. Then, as the insert in Fig. 21 illustrates, the imposed free-field displacements on the spring supports produce a zero external force and a zero external moment!

Notice also that for $\beta_0 < 6$, the response $(\eta_{\text{eff}}, \theta_{\text{eff}})$ of the caisson plotted versus β_0 is independent of the caisson slenderness. At higher frequencies this is not exactly the case, although the undulations of the three curves follow a similar pattern, with peak values in the studied range occurring
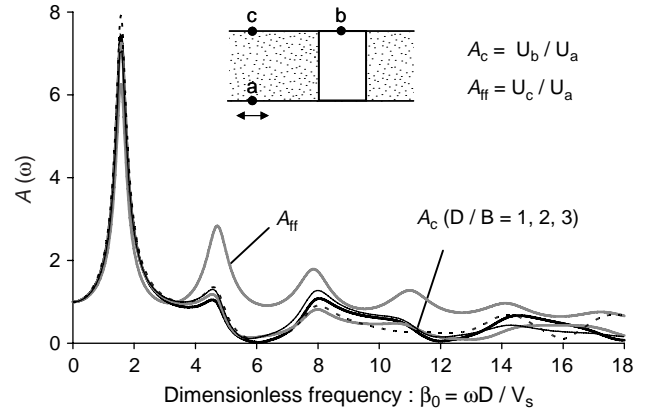

Fig. 22. Comparison of the transfer functions (amplification ratios) between top ($z = 0$) and base ($z = D$) displacement amplitudes for the free-field ($\mathcal{A}_{\text{ff}}$) and the caisson ($\mathcal{A}_{\text{c}}$). Square caisson with slenderness ratios $D/B = 1$, 2 and 3. Solution for $D/B = 1$ using Novak's method gives the spring and dashpot curves (dotted lines).

at $\beta_0 \approx 3$, 9 and 15. These values correspond to wave lengths of about 0.5, 1.5 and 2.5D, respectively, at which, as the insert illustrates, the free-field displacements impose a large unbalanced moment on the caisson supports, inducing eventually its peak response.
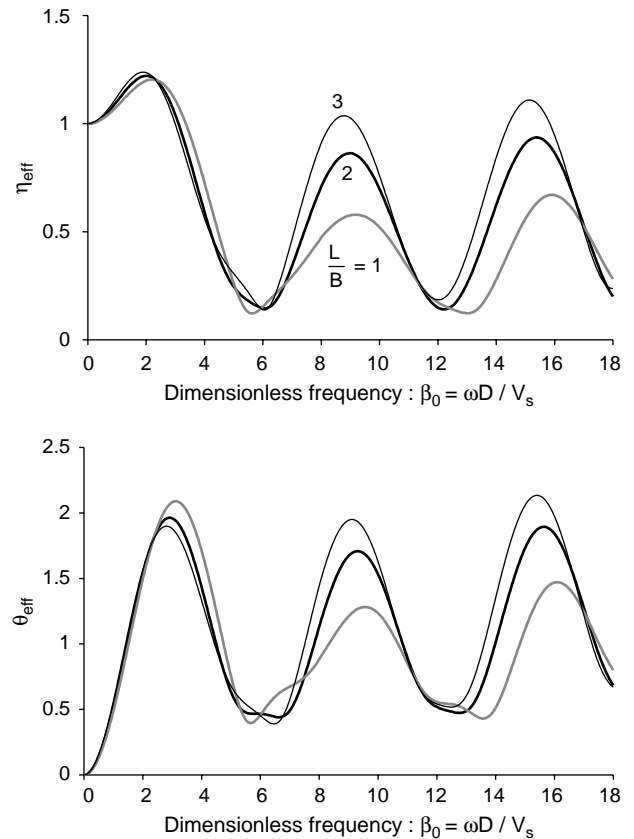

Fig. 23. Effect of the caisson shape ($L/B = 1$, 2, 3) on the effective displacement (top) and rotation (bottom) ratios atop a rectangular caisson with slenderness ratio $D/B = 2$. The caisson is fully embedded in a homogeneous halfspace. The kinematic loading has been derived from the free-field response analysis of a soil column supported by a deformable bedrock of impedance ratio $\alpha = 0.07$.

Finally notice that whereas in general $\eta_{\text{eff}} < 1$, at low frequencies ($\beta_0 \leq 3$ approximately), η_{eff} reaches values up to 1.25.

This conclusion is further verified in Fig. 22 where a comparison between the free-field and caisson 'amplification' ratios (also called transfer functions) is portrayed. Finally, the influence of the aspect ratio *L/B* on the kinematic response of the caisson (in the direction of the *D*) is illustrated in Fig. 23. Observe that *L/B* plays an important role only at high frequencies.

8. Conclusions

A Winkler model with four types of generalized springs is presented for the lateral static and dynamic response of rigid caissons in a homogeneous elastic soil. The spring and dashpot moduli, calibrated using the elastic theory of rigid embedded foundations, model the complex stress distribution along the shaft of square, rectangular or circular caisson plan shapes. The predictions of the model compare to results of 3D-finite element analysis. It is then utilized to study parametrically the response of a rectangular caisson subjected to (a) lateral dynamic loading at the top, and (b) kinematic loading due to vertical seismic shear wave propagation. Despite its simplicity the model is capable of capturing the important phenomena of the problem, including the wave filtering effect at frequencies above the first natural frequency of the soil.

The versatility of the model makes it easy to extend it to the most interesting cases inhomogeneous and nonlinear soil. This is done in the two companion papers [1,2].

Appendix A. Regarding the derivation of Eq. (33)

The equilibrium of a kinematically loaded rigid caisson with respect to its base gives

$$-m\ddot{u}_c(t) - \int_0^d \tilde{k}_x(z)[u(z,t) - U_{\text{ff}}(z,t)]\mathrm{d}z - \tilde{K}_h[u_b(t) - U_{\text{ff}}(0,t)] = 0$$

(A1)

for the horizontal forces, and

$$-J_c\ddot{\theta}_c(t) - m\frac{D}{2}\ddot{u}_c(t) - \int_0^d \tilde{k}_x(z)[u(z,t) - U_{\text{ff}}(z,t)]z\,\mathrm{d}z$$

$$-\int_0^d \tilde{k}_\theta(z)[\theta_c(t) - U'_{\text{ff}}(z,t)]\mathrm{d}z - \tilde{K}_r[\theta_c(t) - U'_{\text{ff}}(0,t)]$$

$$= 0$$

(A2)

for the overturning moments. Using Eqs. (2) and (4), and transferring all the terms of U_{ff} and U'_{ff} to the right side of Eqs. (A1) and (A2), Eq. (33) is obtained.

References

[1] Gerolymos N, Gazetas G. Development of Winkler model for static and dynamic response of caisson foundations with soil and interface nonlinearities. Soil Dyn Earthq Eng, in press, doi: 10.1016/j.soildyn.2005.12.002.

[2] Gerolymos N, Gazetas G. Static and dynamic response of massive caisson foundations with soil and interface nonlinearities—validation and results. Soil Dyn Earthq Eng, in press, doi: 10.1016/j.soildyn.2005.12.001.

[3] Anastasopoulos I, Gerolymos N, Gazetas G. Possible collapse reasons of an access span of the nishinomiya-ko bridge: kobe 1995. Proceedings of the fourth hellenic conference on geotechnical engineering, Athens, vol. 2; 2001. p. 83–90.

[4] Tajimi H. Dynamic analysis of a structure embedded in an elastic stratum. Proceedings of the fourth world conference on earthquake engineering, Santiago, Chile; 1969.

[5] Beredugo YO, Novak M. Coupled horizontal and rocking vibration of embedded footings. Can Geotech J 1972;9(4):477–97.

[6] Kausel E, Roesset JM. Dynamic stiffness of circular foundations. J Eng Mech Div ASCE 1975;101(6):770–85.

[7] Dominguez J. Dynamic stiffness of rectangular foundations. Research Report R78-20. Department of Civil Engineering, Massachusetts Institute of Technology, Cambridge; 1978.

[8] Tassoulas JL. Elements for the numerical analysis of wave motion in layered media. Research Report R81-2. Department of Civil Engineering, Massachusetts Institute of Technology, Cambridge; 1981.

[9] Karabalis DL, Beskos DE. Dynamic response of 3-D embedded foundations by the boundary element method. Comput Methods Appl Mech Eng 1986;56:91–119.

[10] Mitta A, Luco JE. Dynamic response of a square foundation embedded in an elastic half space. Soil Dyn Earthq Eng 1989;8.

[11] Tajirian FF, Tabatabaie M. Vibration analysis of foundations on layered media. In: Gazetas G, Selig ET, editors. Vibration problems in geotechnical engineering. New York: ASCE; 1985.

[12] Harada T, Kubo K, Katayama T. Dynamic soil–structure interaction analysis by continuum formulation method. Report of the Institute of Industrial Science, vol. 29. The University of Tokyo; 1981 [issue no. 5].

[13] Saitoh M. Effective seismic motion of caisson and pile foundation. RTRI Rep 2001;46.

[14] Gazetas G, Dobry R, Tassoulas JL. Vertical response of arbitrarily shaped embedded foundations. J Geotech Eng ASCE 1985;111(6):750–71.

[15] Gazetas G, Tassoulas J. Horizontal stiffness of arbitrarily shaped embedded foundations. J Geotech Eng ASCE 1987;113(5):440–57.

[16] Gazetas G, Tassoulas JL. Horizontal damping of arbitrarily shaped embedded foundations. J Geotech Eng ASCE 1987;113(5):458–75.

[17] Fotopoulou M, Kotsanopoulos P, Gazetas G, Tassoulas JL. Rocking damping of arbitrarily-shaped embedded foundations. J Geotech Eng ASCE 1989;115(4):473–89.

[18] Gazetas G. Formulas and charts for impedances of surface and embedded foundations. J Geotech Eng ASCE 1991;117(9):1363–81.

[19] Gadre A, Dobry R. Lateral cyclic loading centrifuge tests on square embedded footing. J Geotech Geoenviron Eng ASCE 1998;124(11):1128–38.

[20] Davidson HL. Laterally loaded drilled pier research. Research Report, Electric Power Research Institute, vol. 2. Pennsylvania: Gai Consultants, Inc.; 1982.

[21] Mylonakis G, Gazetas G, Nikolaou S. Footings under seismic loading. analysis and design issues with emphasis on bridge foundations. Soils Dyn Earthq Eng 2005.

[22] Makris N, Gazetas G. Dynamic pile–soil–pile interaction. Part II. Lateral and seismic response. Earthq Eng Struct Dyn 1992;21:145–62.

[23] Mylonakis G. Elastodynamic model for large-diameter end-bearing shafts. Soil Found 2001;41(3):31–44.

[24] Novak M, Nogami T, Aboul-Ella F. Dynamic soil reactions for plane strain case. J Eng Mech Div ASCE 1978;104(4):953–9.

[25] Kramer S. Geotechnical earthquake engineering. Englewood Cliffs, NJ: Prentice-Hall; 1996.